CHEMISTRY OF MATERIALS

pubs.acs.org/cm

Article

The Length of Molecular Tethers Can Be Used to Control the Structure and Electronic Properties of Stapled Supramolecular Polymers

Victor Paulino, Danielle M. Cadena, Kaixuan Liu, Arindam Mukhopadhyay, Sean T. Roberts,* and Jean-Hubert Olivier*

Cite This: *Chem. Mater.* 2022, 34, 6518−6528

Read Online

ACCESS | Metrics & More | Article Recommendations | Supporting Information

ABSTRACT: Formed through equilibrium-driven processes, π-conjugated supramolecular polymers (π-SPs) are equipped with electronic structures that are primarily governed by van der Waals interactions between repeating units. Consequently, the structure−function relationships of these materials are extremely sensitive to changes in temperature, solvent composition, and building block concentration. These experimental constraints not only render the processing of π-SPs challenging but also restrain the molecular toolkit to tailor, by design, their ground, and excited-state electronic structures without completely overhauling the structural design of their repeating units. Herein, we show that stapling initially formed π-SPs with a short molecular tether delivers electronically and structurally robust nanoscale objects whose ground-state electronic structures are insensitive to changes in temperature, thus making the tethering component a versatile synthetic handle to tailor the functions of π-SPs post assembly. Ultrafast transient absorption measurements that track the excited-state dynamics of stapled structures further highlight their structural rigidity. Photoexcitation of the stapled π-SPs generates excited states with mixed Frenkel exciton and charge-transfer character. Notably, we find that the charge-transfer contributions to these states can be enhanced by increasing the structural rigidity of the π-SPs, providing a potential pathway for separating charges for light-harvesting applications. Deviating from conventional supramolecular tools, our reported post-assembly modification strategy highlights a new set of design principles that can guide the molecular engineering of materials with designer electronic properties for applications in light-harvesting, photocatalysis, and organic electronics.

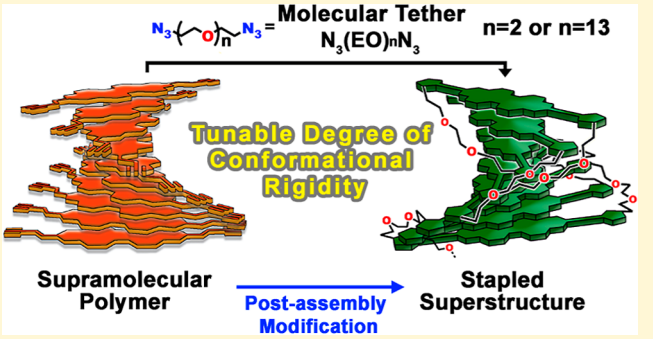

INTRODUCTION

Nature has mastered strategies to precisely control the conformation of non-covalent superstructures by constraining the arrangement and interaction modes of functional building blocks.[1,2] Photosystems are a perfect example of natural engineering where the spatial organization of chromophores is enforced by protein scaffolds that consequently enable these chromophores to form delocalized excitonic states and transport energy over long distances.[3−5] Synthetic strategies that restrict the conformation of non-covalent, π-conjugated assemblies with the level of precision exhibited by natural systems are scarce, yet essential to pioneer material compositions relevant to solar energy capture, conversion, and storage.[6−10]

Conventional approaches to modulate the structure−function relationships of artificial dye assemblies, also named π-conjugated supramolecular polymers (π-SPs), have primarily focused on the design and synthesis of repeating units.[11−13] Seminal contributions have unambiguously demonstrated that subtle structural changes implemented on the side chains of chromophore building blocks can dramatically impact the ground- and excited-state electronic properties of molecular aggregates.[14] Dispersion forces between repeating units closely govern the magnitude of Coulombic and charge transfer (CT)-mediated couplings.[15−17] These electronic parameters have been shown to dictate the formation of excimer states,[18,19] singlet fission,[20−23] and symmetry-breaking charge separation.[24−26] While these pioneering studies provide important sets of design principles, challenges persist in the field. Specifically, our ability to control the electronic coupling between building blocks in π-SPs is limited as dispersion forces remain the foremost parameter that regulates their assembly.[27−31] The inherent advantage of constructing π-SPs through equilibrium-driven processes is also the origin of the

Received: May 4, 2022
Revised: June 18, 2022
Published: July 12, 2022

major limitation of these materials: they are notoriously fragile. Minor changes to parameters such as solvent dielectric,[32,33] temperature,[34,35] and building block concentration perturb weak interactions,[36,37] consequently disrupting emergent electronic properties of interest needed for modular platforms with potential applications in solar energy harvesting and transduction.

Strategies that can address this limitation have recently been explored in the context of biopolymers. In particular, peptide stapling is a powerful technique to stabilize secondary structures such as α-helix motifs.[38,39] This synthetic method has been leveraged to engineer robust, nanoscale objects that preserve their native conformations as temperature or solvent composition varied.[40,41] Two strategies exist in peptide stapling: one-component stapling relying on intramolecular reactions between complementary functional groups flanked on amino acids that are integral parts of a peptide backbone,[42] and two-component stapling which employs extrinsic modification of peptide backbones with external molecular tethers,[43] thereby allowing for a high degree of modularity in the design of peptide structures.[44] Two-component stapling can open new avenues for controlling the electronic and optical properties of π-SPs through selection of distinct molecular tethers.

Similar to one-component stapling, the covalent cross-linking of supramolecular architectures has been developed to stabilize the structure of non-covalent assemblies. Seminal studies have reported post-assembly modification of non-covalent aggregates using ring-opening metathesis and radical polymerizations,[45−48] leading to formation of organic nanotubes,[49,50] micelles,[51,52] and hydrogels in solution.[53] In this approach, polymer precursor functionalities are incorporated into molecular building blocks that assemble into non-covalent supramolecular structures. Post-assembly, these functionalities are leveraged to rigidify the emergent superstructures. While this approach can deliver materials equipped with structural and electronic properties that differ from those of their parent non-covalent assemblies, challenges persist. In particular, the insertion of reactive precursor functionalities (*i.e.*, butadiyne, 1,3-diene, and norborene) onto molecular building blocks limits this approach as it (1) can perturb the initial aggregation properties, (2) hinders the synthetic viability of the precursor building blocks through extensive reaction steps, and (3) limits the implementation of novel functions that would be made possible by a two-component stapling approach.

In prior work, we reported the first use of a two-component stapling procedure to form tethered superstructures from water-soluble π-SPs.[54] While this initial contribution established a methodology to tether supramolecular polymers, it did not explore the extent to which stapler structure can be used to regulate the structure and electronic properties of stapled π-SPs. Herein, we demonstrate that stapling perylene bisimide (PBI)-derived supramolecular polymers with a molecular tether that features a low degree of structural freedom delivers a structurally and electronically robust superstructure, **PBI-Stap-2** (Figure 1A), whose ground-state electronic structure is insensitive to environmental perturbations, such as changing temperature or solvent. Noteworthy, our findings contrast those reported previously for an assembly stapled with a longer, more flexible molecular tethers, $\mathbf{N_3(EO)_{13}N_3}$ (Figure 1A),[54] which was found to possess a structure sensitive to perturbations of its local environment. Using ultrafast pump-probe transient absorption (TA) spectroscopy, we demonstrate that the structural rigidity enforced by the short covalent tethers of **PBI-Stap-2** rebalances the short- and long-range electronic coupling between PBI units, giving rise to delocalized excitonic states with a more pronounced degree of CT character than those formed in non-covalent PBI assemblies. This study delineates the first example showing that molecular tethers can be used as synthetic handles to rigidify the electro-active cores of stapled supramolecular polymers. Compellingly, our approach opens new opportunities to control the ground- and excited-state electronic properties of non-covalent assemblies without modifying the chemical compositions of π-conjugated repeating units.

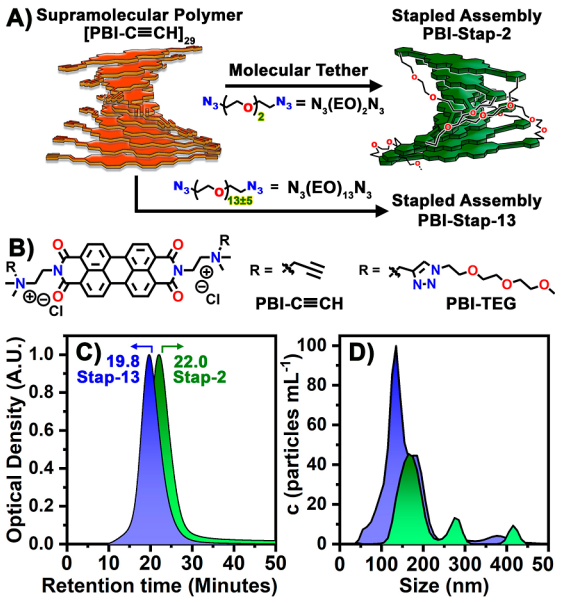

Figure 1. (A) Tethering the parent non-covalent assembly $[\text{PBI-C}{\equiv}\text{CH}]_{29}$ with the molecular tethers $N_3(EO)_2N_3$ and $N_3(EO)_{13}N_3$ delivers the stapled superstructures PBI-Stap-2 and PBI-Stap-13, respectively. (B) Molecular structures of the parent building block PBI-C≡CH and the control unit PBI-C_2Am-TEG. (C) Gel permeation chromatograms comparing the retention time of the PBI-Stap-2 (green) and PBI-Stap-13 (blue) superstructures in 50% MeCN/50% water as the mobile phase (see Section 4 of Supporting Information for experimental details). (D) Hydrodynamic radii of the PBI-Stap-2 (green) and PBI-Stap-13 (blue) assemblies interrogated using nanoparticle tracking analysis (NTA). Solvent = 100% water.

RESULTS AND DISCUSSION

Synthesis and Structural Characterization of PBI-Stap-2. A gel permeation chromatogram of **PBI-Stap-2** is shown in Figure 1C and compared to that reported for **PBI-Stap-13**. Structural differences exist as the assembly tethered with the short linker unit $\mathbf{(EO)_2}$ is characterized by a longer retention time (22 min). While **PBI-Stap-2** demonstrates a weight-average molecular weight (M_w = 18,000 g/mol) that is smaller than that reported for **PBI-Stap-13** (M_w = 31,700 g/mol), these M_w's indicate that an average of 22 and 23 stacked PBI units comprise the **PBI-Stap-2** and **PBI-Stap-13** superstructures, respectively. Because these two stapled assemblies are built from identically stacked PBI cores and originate from the common $\mathbf{[PBI\text{-}C{\equiv}CH]_{29}}$ precursors, as shown in Figure 1C, the discrepancy in their measured M_w's originates from the structural difference of their peripheral ethylene oxide units. It is fair to assume that the shorter molecular tether exists under an extended conformation that occupies a smaller volume than

https://doi.org/10.1021/acs.chemmater.2c01353
Chem. Mater. 2022, 34, 6518−6528

the longer, more flexible tether that allows the formation of more solvated, less constrained conformations of the polyethylene oxide units.

It is interesting to correlate the number of repeating units in the tethered assemblies with that comprised in the non-covalent parent π-SP, **[PBI-C≡CH]$_{29}$**. The aggregation mechanism and the average number of building blocks of this non-covalent precursor have been elucidated previously using an isodesmic supramolecular polymerization mechanism.[54] At the 1 mM concentration used to perform the stapling reaction, the **PBI-C≡CH** units, as shown in Figure 1B, exist as a non-covalent π-SP built from an average of 29 repeating units. The fact that the stapled **PBI-Stap-13** and **PBI-Stap-2** assemblies feature 23 and 22 repeating units, respectively, indicates that the tethers **$N_3(EO)_{13}N_3$** and **$N_3(EO)_2N_3$** enable the stapling step to operate at an ∼80% yield. Note that because the **PBI-Stap-2** and **PBI-Stap-13** superstructures feature ethylene oxide moieties at the periphery of the PBI redox cores, we employ non-covalent assemblies built from the **PBI-TEG** monomer, as shown in Figure 1B, abbreviated as **PBI-Non-Cov**, as a control in measurements below to assess the impact that stapling has on the structure and dynamics of the tethered superstructures. As shown previously, the **PBI-TEG** and **PBI-C≡CH** building blocks share similar self-assembly properties in water solution.[54]

NTA was performed to elucidate the approximate particle size distribution of stapled PBI derivatives in aqueous media and assess whether there is any correlation between stapler length and the hydrodynamic radius (d_h) of the resulting π-SPs. We acknowledge that the acquired measurements are strictly approximations as the one-dimensional (1D) nature of the tethered PBI structures contrasts in shape with the round SiO_2 nanoparticles (d_h ∼100 nm) used as internal calibration standards,[55] and resolution decreases for nanoparticles with higher aspect ratios.[56,57] Despite these limitations, similar techniques also employed in the size determination of spherical nanoparticles, such as dynamic light scattering, have been used to qualitatively characterize and track the formation of non-spherical organic hierarchical materials in solution.[58−60] Capitalizing on this prior work, NTA was employed to gather qualitative information on the relative size distribution of stapled superstructures against the non-covalent control. For the **PBI-Stap-13** superstructures, particles with a hydrodynamic radius of 149 ± 11 nm were recorded (Figure 1D). Comparably, the **PBI-Stap-2** superstructures showcase a d_h of 155 ± 35 nm. These values fall within the accepted range for standard nanoparticles in solution.[61,62] Furthermore, we measured particle concentrations within the same order of magnitude for both polymer systems, implying comparable solvation of the resulting nanoparticles.

While the d_h recorded for the tethered PBI assemblies indicates the existence of particles that are larger than those measured using gel permeation chromatography (GPC), it is important to note that GPC measurements are performed in 50% CH_3CN in H_2O, whereas NTA is performed in pure H_2O. In the latter solvent system, interaction of the stapled assemblies through their ethylene glycol domains may initiate formation of aggregated particles that do not exist in the solvent mixture used for GPC experiments. The fact that both tethered PBI assemblies exhibit similar d_h values, even if partially aggregated, highlights their comparable average stack lengths regardless of the stapler used to connect PBIs. In sharp contrast with the stapled assemblies, NTA measurements of the control species **PBI-Non-Cov** were saturated by fluorescence arising from PDI building block monomers in solution, making these measurements unreliable (Section 5, Supporting Information).

As shown by scanning electron microscopy (SEM) images in Figure 2A, the **PBI-Stap-2** superstructure drives the formation of hierarchical 1D objects in the solid state whose length spans tens of micrometers. This solid-state morphology differs dramatically from that observed for the non-covalent control assembly, **PBI-Non-Cov**, which forms globular amorphous domains. Please refer to Figures S22−S24 and the associated discussion. Additionally, the solid-state morphologies of **PBI-Stap-2** resemble those previously reported for the **PBI-Stap-13** analogue. While this finding indicates that molecular tethers flanked on the stapled superstructures are an important structural parameter that initiates the formation of hierarchical domains in the solid state, no drastic differences are observed between the two stapled assemblies at microscale dimensions (Section 8, Supporting Information).

To glean further insights at the nanoscale level, atomic force microscopy (AFM) was employed. Figure 2B,C reveals the existence of thin, organic nanowires, which represent an intermediate aggregated state that may evolve into the hierarchical microscale 1D objects elucidated by SEM. We postulate that they originate from the interaction of the tethered **PBI-Stap-2** assemblies along a 1D axis. Please refer to Section 9 of Supporting Information for more details. Note, these captured nanoscale wires are exclusively formed from a drop cast water solution. While our superstructures are fully dispersed in 1:1 CH_3CH/H_2O solutions, NTA suggests that some aggregation of superstructures occurs when they are dissolved in H_2O. Statistical analysis was performed on more than 100 cross-section profiles, the results of which are shown in Figure 2D. The average diameter of the **PBI-Stap-2**

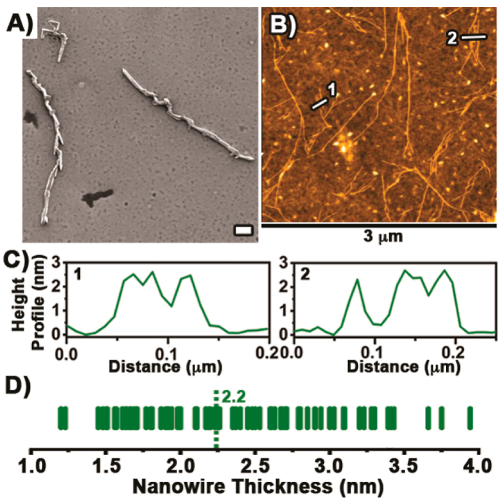

Figure 2. Solid-state morphologies of the **PBI-Stap-2** acquired *via* scanning electron microscopy (A) and atomic force microscopy (B). The height profiles in C have been recorded along the white lines shown in B. The solid-state samples are obtained by drop casting the respective tethered superstructures solvated in pure water on silicon supports. Scale bars in A correspond to 10 μm. (D) Distribution of nanowire thicknesses recorded for the **PBI-Stap-2** (green) superstructures. The dotted line represents the average thickness. Please see Section 7 of Supporting Information for more details.

https://doi.org/10.1021/acs.chemmater.2c01353
Chem. Mater. 2022, 34, 6518−6528

nanowires is 2.2 nm and contrasts that measured for wires formed by **PBI-Stap-13** (d = 3.4 nm). Please note that the diameter assessed for the **PBI-Stap-13** assemblies in this study is modestly smaller than that which we previously reported (4 ± 0.5 nm) due to the use of a more accurate statistical analysis approach (Section 7, Supporting Information).[54] Our observation that stapled assemblies built with the $N_3(EO)_2N_3$ tether are thinner than those built from $N_3(EO)_{13}N_3$ confirms that the stapled PBI cores feature structurally different outer layers.

Ground-State Electronic Spectral Properties are Intimately Related to the Structure of the Tethers. The ground-state electronic absorption spectra shown in Figure 3A demonstrate that even at an elevated temperature (368 K) where the control non-covalent supramolecular polymer **PBI-Non-Cov** largely breaks up into PBI monomers, as evidenced by the well-resolved 0−0 and 0−1 vibronic transition (Figure 3A), **PBI-Stap-2** superstructures remain in an aggregated state, as signaled by the ratio of their 0−0 to 0−1 vibronic transition that is well below the 1.25 value characteristic of molecularly individualized PBI units.[63,64] The variable-temperature spectra recorded for the **PBI-Stap-2** superstructures (Figure 3B) show minor spectroscopic perturbation as the temperature is tuned from 274 to 368 K, which confirms the formation of structurally robust nanoscale objects. Indeed, the only spectroscopic observable over the 274-to-368-K temperature range is a minor increase in the amplitude of the 0−1 vibronic transition as the temperature is lowered with a concomitant decrease in the 0−0 transition.

To interrogate the extent to which the structure of the molecular tethers used to staple the parent supramolecular polymer act on the interchromophore interactions, the excitonic coupling (J_{12}) between PBI units, which measures

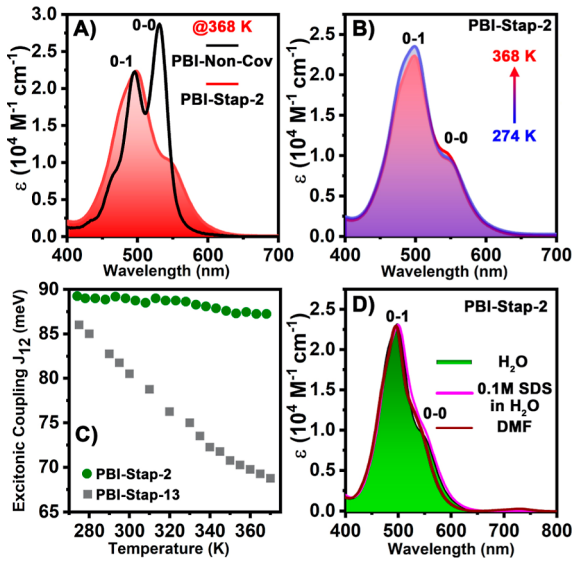

Figure 3. (A) Absorption spectra at 368 K of **PBI-Stap-2** and **PBI-Non-Cov** in D_2O. (B) Temperature-dependent electronic absorption spectra recorded for the stapled **PBI-Stap-2** assembly in D_2O. (C) Excitonic coupling (J_{12}) as a function of temperature for **PBI-Stap-2** (green ●) inferred from their electronic absorption line shape. The J_{12} calculated for PBI-Stap-13 (gray ■) is shown for comparison. (D) Solvent-dependent electronic absorption spectra of the **PBI-Stap-2** superstructures recorded at 293 K. Extinction coefficients are reported per PBI unit.

the exciton absorption line width that is sensitive to the degree of interaction between neighboring chromophores in the assembly, has been calculated as a function of temperature using a model developed by Spano and co-workers that has been shown to successfully reproduce spectra of coupled PBI aggregates (Figure 3C).[16,65] Compellingly, **PBI-Stap-2** shows less than a 3% decrease of its inter-PBI excitonic coupling as the temperature is changed from 274 to 368 K. This finding starkly contrasts that previously reported by us for **PBI-Stap-13** (gray squares, Figure 3C), which shows a decrease in J_{12} of more than 18% over an identical temperature range. For the sake of clarity, Figure S31 compares the temperature-dependent spectra recorded for **PBI-Stap-2** and **PBI-Stap-13** assemblies. Spectra of PBI molecular crystals wherein molecules are arranged into 1D stacked columns have shown that sub-Ångstrom displacements between PBI molecules can significantly alter their electronic coupling.[65−68] As such, the negligible decrease in excitonic coupling recorded for stapled **PBI-Stap-2** assemblies points to negligible perturbation of their structure as the temperature varied over the probed range (274−368 K). Our data underscore that the short $N_3(EO)_2N_3$ tether promotes the formation of highly rigid nanoscale objects that are stiffer than those constructed from the parent non-covalent assembly using a longer $N_3(EO)_{13}N_3$ molecular tether.

Solvent-dependent ground-state electronic absorption spectra acquired for **PBI-Stap-2** superstructures reveal they are also resistant to changes in their solvation environment. While the non-covalent control **PBI-Non-Cov** forms an aggregated state in water, in DMF these aggregates dissolve to yield PBI monomers, as evidenced by electronic absorption spectra of their $S_0 \rightarrow S_1$ transition that show a vibronic progression indicative of PBI monomers (Figure S30).[69] A similar observation is made when using a sodium dodecyl sulfate (SDS) surfactant that exfoliates and individualizes aggregated PBI units in water.[46] In sharp distinction, **PBI-Stap-2** demonstrates spectroscopic signatures (Figure 3D) that are unaffected by changing solvation conditions (H_2O *vs* DMF) or the addition of SDS surfactants ([SDS] = 0.1 M). The absence of significant variance in the absorption spectra of **PBI-Stap-2** attests to the ability of our stapling methodology to achieve structures with a high degree of rigidity as varying solvent conditions do not perturb, to a measurable degree, the J_{12} between neighboring units within a polymer strand (Figures S29 and S30). The placement of short, covalent tethers in the periphery of **PBI-Stap-2** superstructures prevents the dismantling of their stacked PBI cores and enforces excitonic coupling in solvation environments that overcome dispersion forces. In essence, the solvent-dependence measurements are in fair agreement with the temperature-dependence studies, demonstrating that changes in interchromophore interactions within stapled assemblies are negligibly impacted by their external environment. This differs significantly from behavior exhibited by the non-covalent control **PBI-Non-Cov** and **PBI-Stap-13** superstructure, which show evidence of structural changes upon heating (Figure 3C).

Solution-Phase Potentiometric Properties Confirm Increasing Superstructure Rigidity. The potentiometric properties recorded for the stapled **PBI-Stap-2** construct are compared to those measured for **PBI-Stap-13** and the non-covalent control **PBI-Non-Cov** assembly, and reveal that, as initially hypothesized, the molecular tethers act as a structural handle to regulate the electronic structures of the stapled

https://doi.org/10.1021/acs.chemmater.2c01353
Chem. Mater. 2022, 34, 6518−6528

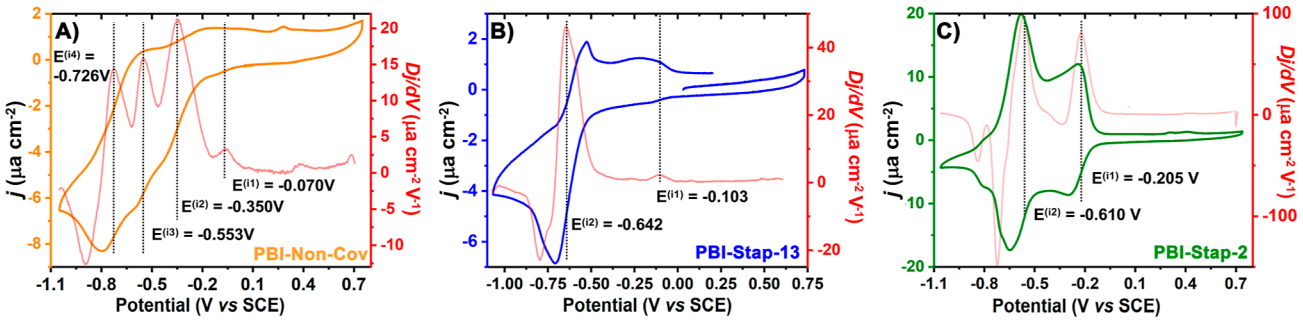

Figure 4. Solution-phase CVs recorded for the (A) control, non-covalent assembly **PBI-Non-Cov**, the (B) stapled **PBI-Stap-13** superstructure, and the (C) stapled **PBI-Stap-2** superstructure. The first derivative of the voltammograms are shown as light red traces and allow estimation of the inflection potentials ($E^{(in)}$). Experimental conditions: [PBI] = 500 μM; solvent = argon-degassed water; atmosphere = argon; temperature = 20 °C; working electrode = glassy carbon; counter electrode = platinum; supporting electrode = Ag/AgCl (3 M NaCl); scan rate = 100 mV s^{-1}; internal reference = dicarboxylicacidferrocene.

assemblies. To provide an insightful discussion, we start summarizing the electrochemical properties of the **PBI-Non-Cov** and **PBI-Stap-13** assemblies, which are leveraged to highlight the electronic properties of the novel **PBI-Stap-2** assembly.

The cyclic voltammogram (CV) recorded for the **PBI-Non-Cov** assembly (Figure 4A) shows ill-resolved waves observed when sweeping toward the cathodic and anodic potentials that are hallmarks of irreversible electrochemical systems.[70] The inflection potentials, $E^{(in)}$, calculated during the cathodic sweep (−1.05 V) highlight the existence of at least four reduction potentials within the −0.070 to −0.726 V potential window. These values correspond to progressive n-doping of the control assembly.[69,71] This irreversible electrochemical behavior observed for the control, non-covalent **PBI-Non-Cov** assembly is suggestive of both conformational heterogeneity within the structure, which is a well-known attribute of non-covalent assemblies, as well as structural rearrangement of monomers within the assembly that occurs upon electron injection.

A CV of **PBI-Stap-13** is plotted in Figure 4B and shows that the potentiometric properties of this superstructure bear both similarities and notable differences to those of **PBI-Non-Cov**. Irreversible electrochemical signals characterize the **PBI-Stap-13** superstructure where only two distinct inflection potentials, $E^{(i1)}$ = −0.103 V and $E^{(i2)}$ = −0.642 V, are measured. Notably, the **PBI-Non-Cov** assembly and **PBI-Stap-13** superstructure share a similar first reduction potential $E^{(i1)}$. This observation underscores that some of the ground-state electronic properties characteristic of the non-covalent assembly are translated to the **PBI-Stap-13** superstructure. However, the second inflection potential measured for **PBI-Stap-13**, $E^{(i2)}$ = −0.642 V, differs from the values estimated for the non-covalent assembly ($E^{(i3)}$ = −0.533 V and $E^{(i4)}$ = −0.726 V). This difference indicates that at a higher level of n-doping, the electronic structures of these two nanoscale objects diverge. This finding highlights the non-innocent role played by the covalent tether of the **PBI-Stap-13** superstructure. At modest n-doping levels, the $\mathbf{N_3(EO)_{13}N_3}$ tethers have little to no impact on the low-lying electronic states delineated by the stacked PBI cores. For the control **PBI-Non-Cov** assembly, as the level of n-doping increases during the sweep toward cathodic potentials, Coulombic repulsion between n-doped PBI units is expected to significantly perturb the conformation of the non-covalent architectures. However, the existence of covalent tethers in the **PBI-Stap-13** superstructure can limit the degree of structural modification and engender formation of electronic states that differ from those of the non-covalent **PBI-Non-Cov** assembly.

When compared to the $\mathbf{N_3(EO)_{13}N_3}$ molecular tether, the shorter, more rigid $\mathbf{N_3(EO)_2N_3}$ linker featured in **PBI-Stap-2** has the greatest impact on the electronic properties of its stacked redox active PBI cores. As seen in Figure 4C, the CV of this nanoscale object reveals the existence of a reversible electrochemical system with two distinct reduction potentials centered at $E^{(i1)}$ = −0.205 V and $E^{(i2)}$ = −0.610 V. The reversible behavior exhibited by **PBI-Stap-2** contrasts that seen for **PBI-Stap-13** and suggests **PBI-Stap-2** forms more discrete electronic states upon n-doping as a result of the structural rigidity enforced by its short stapling units. Furthermore, the fact that the first reduction potential of **PBI-Stap-2** ($E^{(i1)}$ = −0.205 V) is catholically shifted by ∼100 mV with respect to that measured for **PBI-Stap-13** ($E^{(i1)}$ = −0.103 V) indicates that the ground-state electronic structure of the former impedes electron injection. This destabilization could originate from different degrees of through-space PBI radical ion stabilization that exist in the **PBI-Stap-2** assemblies. In addition, the structural rigidity conferred by the short molecular linker in **PBI-Stap-2** is expected to favor a solvation environment that differs from that of **PBI-Stap-13**. Consequently, the ability of solvent molecules to screen negative charge carriers injected into each structure is likely to differ, which can rationalize the differences we observe in their first reduction potentials. To complement this explanation, we cannot rule out that the increased structural rigidity of **PBI-Stap-2** may restrict the access to conformations that can facilitate electron injection at less negative cathodic potentials.

Spectroelectrochemistry. Spectroscopic signatures of the n-doped species formed by **PBI-Stap-2** as a function of applied potential are compared to those recorded for **PBI-Non-Cov** and **PBI-Stap-13** and provide additional evidence that the molecular tethers modulate the electronic structure of the redox-active PBI cores of each assembly. The results of spectroelectrochemical measurements performed on these solvated nanoscale objects in an aqueous medium are shown in Figures 5 and S33−37. As seen in Figure S33, the application of a cathodic potential of −0.15 V promotes the formation of spectroscopic features reminiscent of PBI radical anions for the three constructs. For **PBI-Stap-13** and **PBI-Non-Cov**, increasing the potential to −0.25 V leads to the rise of a broad NIR transition centered at 1700 nm (Figure 5A) that has been recently reported to indicate the formation of radical π-anion aggregates.[72,73] As previously reported, non-

https://doi.org/10.1021/acs.chemmater.2c01353
Chem. Mater. 2022, 34, 6518−6528

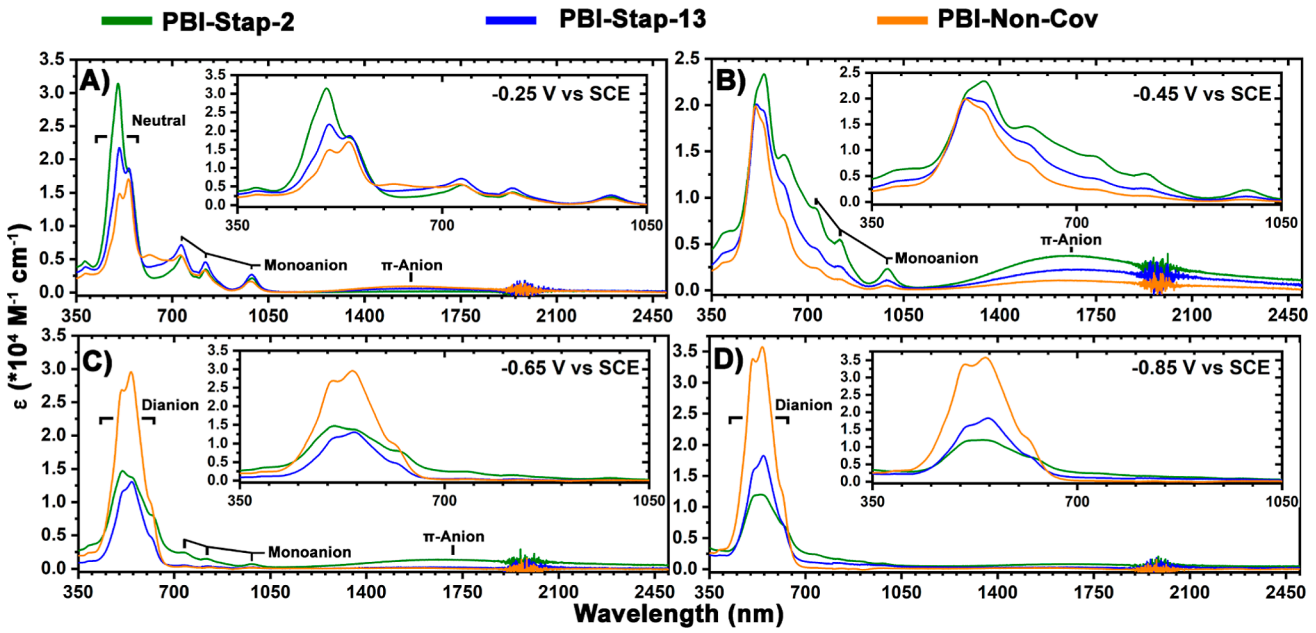

Figure 5. Electronic absorption spectra measured as a function of applied cathodic potentials that characterize the spectroscopic signatures of the n-doped forms of non-covalent **PBI-Non-Cov** assemblies (orange trace), **PBI-Stap-13** superstructures (blue trace), and the **PBI-Stap-2** superstructures (green trace): (A) −0.25 V *vs* SCE, (B) −0.45 V *vs* SCE, (C) −0.65 V *vs* SCE, and (D) −0.85 V *vs* SCE. Experimental conditions: [PBI] = 500 μM in deuterated water; argon atmosphere; optical pathlength = 1.7 mm; gold-mesh working electrode; temperature = 20 °C; and gold counter electrode. Extinction coefficients are reported per PBI unit.

covalent interactions between rylene monoanion cores in n-doped π-stacks enables the formation of spectroscopic states that originate from singly occupied molecular orbital interactions.[74−77] It is interesting to note that for the **PBI-Stap-2** superstructure, a larger potential of −0.35 V is required to unambiguously detect a spectroscopic signature of radical π-anion aggregates (Figure S34). Additionally, at this potential, the n-doped **PBI-Stap-2** construct is characterized by more sharply resolved absorptive features centered at 990, 818, 732, and 625 nm associated with the PBI monoanion.

Increasing the cathodic potential from −0.35 to −0.65 V (Figures 5B,C, and S35) engenders disappearance of the NIR transitions observed for **PBI-Stap-13** and **PBI-Non-Cov**. We also note the development of absorptive features in the visible spectral window (350−700 nm) that signal formation of electronic states having PBI dianion character (see the Supporting Information for more details). Contrasting this observation, the NIR feature centered at 1700 nm for the **PBI-Stap-2** superstructure persists at −0.65 V (Figure 5C) alongside the absorption bands at 990, 816, and 734 nm. These findings indicate that at a potential (−0.65 V) where both the n-doped **PBI-Stap-13** and **PBI-Non-Cov** constructs have significant dianion character,[78] the n-doped **PBI-Stap-2** superstructure preserves the π-anion stack character. Congruent with steady-state spectroscopy and CV experiments, the structural rigidity imposed by the short molecular tether restricts the conformational changes of the redox active cores needed to form n-doped states with pronounced PBI dianion character.

The lower degree of superstructure reorganization conferred by the shorter, more rigid $\mathbf{N_3(EO)_2N_3}$ linker is further unraveled by comparing spectra of the **PBI-Stap-2** superstructure acquired at −0.85 V to those collected for **PBI-Stap-13** and **PBI-Non-Cov** (Figure 5D). While at this cathodic potential, the control, non-covalent assembly **PBI-Non-Cov** exhibits well-resolved vibronic features centered at 507 and 543 nm that are characteristic of molecularly dissolved PBI dianions, the spectroscopic signature of the n-doped **PBI-Stap-2** superstructure centered at 538 nm is featureless and is characterized by a weaker oscillator strength (f = 0.337, Figure S37). In addition, some reminiscent absorptive features in the NIR spectral window indicate the existence of n-doped states having PBI π-anion character. When compared to the control **PBI-Non-Cov** analogues, the existence of covalent bonds in the **PBI-Stap-2** superstructure prevents the dismantlement of the stacked PBI cores due to electrostatic repulsion, consequently preventing the formation of individualized PBI dianions. This conclusion is also corroborated by the ground-state electronic absorption discussed earlier.

Excited-State Spectra and Dynamics. Femtosecond TA spectroscopy was employed to examine the nature of the excited states formed following photoexcitation of the non-covalent, control assembly and stapled superstructures. Contour plots highlighting TA spectra of the **PBI-Non-Cov** and **PBI-Stap-2** structures are shown in Figure 6A,B, while the TA spectrum of **PBI-Stap-13** is shown in Figure S38 of the Supporting Information. Following photoexcitation at 570 nm, all three structures yield a negative feature between 435 and 525 nm that is attributed to photobleaching of their ground-state absorption. A series of excited-state absorption (ESA) peaks centered at 540, 600, and 720 nm grow simultaneously with the ground-state bleach, suggesting they each arise from a common excited state. The ESA contributions centered at 540 and 720 nm align with the spectroscopic signatures of the electrochemically generated PBI radical anion, $PBI^{\bullet-}$ (Figure S39). Additionally, the long-wavelength feature at 720 nm corresponds well with previous reports of $PBI^{\bullet-}$ photoinduced absorption between 700 and 750 nm in TA spectra.[79−81] The ESA at 600 nm has previously been assigned to the $S_1 \rightarrow S_n$ transition of neutral PBI molecules (^{1}PBI*).[23,82] Figures S41

https://doi.org/10.1021/acs.chemmater.2c01353
Chem. Mater. 2022, 34, 6518−6528

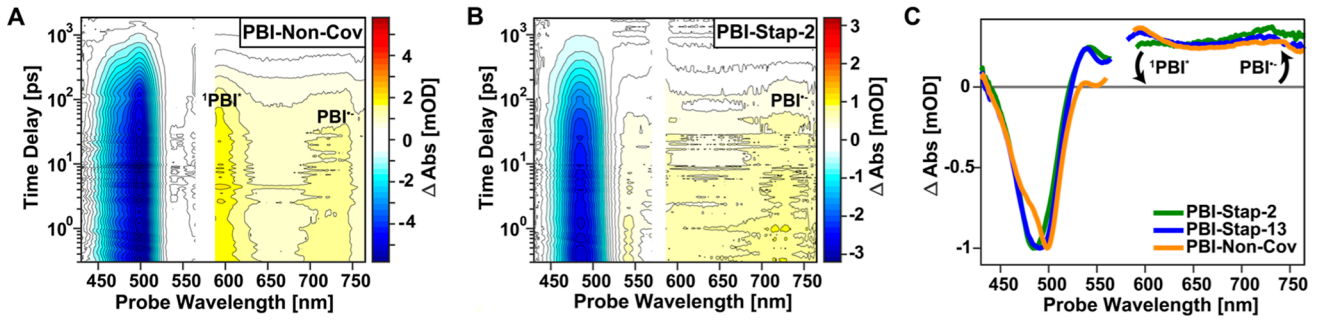

Figure 6. TA contours of the **PBI-Non-Cov** (A) and **PBI-Stap-2** (B) superstructures highlight differences in their excited-state dynamics and the character of the photogenerated states due to tethering the PBI cores. Pump scatter around 570 nm has been subtracted from each contour. Any remaining pump scatter was omitted. (C) TA spectra for the **PBI-Stap-2**, **PBI-Stap-13**, and **PBI-Non-Cov** structures at a time delay, Δt = 2 ps. Changes in the ratio of the ^{1}PBI* and PBI$^{\bullet-}$ ESA bands (600 and 720 nm, respectively) indicate a change in the degree of Frenkel and CT contributions to the excited state formed by each superstructure.

and S42 highlight spectral band shifting in the ^{1}PBI and PBI$^{\bullet-}$ ESA features within the first few picoseconds following photoexcitation, which we assign to structural relaxation of each PBI structure, likely due to a mixture of solvent reorganization and internal nuclear motion (Table S7).

The ESA features of the TA spectra allow us to draw important conclusions regarding the excited-state character of the non-covalent assembly and stapled superstructures. Both ^{1}PBI* and PBI$^{\bullet-}$ ESA features are present shortly after time zero (~300 fs) and decay with lifetimes of 373 ± 10, 406 ± 15, and 235 ± 10 ps for **PBI-Non-Cov**, **PBI-Stap-13**, and **PBI-Stap-2**, respectively (Table 1). This suggests the formation of a single excited state composed of mixed Frenkel exciton and CT character whose excited-state characteristics and dynamics are set by the contribution of each of these diabatic configurations to the excited state.

As intermolecular interactions between PBI units are required for CT, the degree to which each superstructure forms excited states of mixed Frenkel and CT character are expected to reflect differences in the spatial separation between their PBI chromophores. Figure 6C shows normalized TA spectra for all three superstructures at a time delay of 2 ps. These spectra reveal a decrease in ^{1}PBI* ESA intensity and an increase in PBI$^{\bullet-}$ ESA intensity as rigidity is imposed on the system *via* the addition of a covalent tether and a shortening of its length. The integrated ^{1}PBI*/PBI$^{\bullet-}$ peak area ratio (Figure S43) is inversely related to the rigidity of each superstructure, adopting values of 1.21, 1.09, and 0.79 for **PBI-Non-Cov**, **PBI-Stap-13**, and **PBI-Stap-2**, respectively (Table 1). This change in the ^{1}PBI*/ PBI$^{\bullet-}$ peak ratio is consistent with a decrease in PBI chromophore separation moving from the **PBI-Non-Cov** assembly, to the **PBI-Stap-13** and **PBI-Stap-2** superstructures, which increases spatial overlap of the PBI π-systems that enhances the CT character of the excited state formed upon photoexcitation. This enhanced CT contribution to the excited state of each structure is also manifested in their ground-state absorption spectra, which show a progressive line width increase moving from the non-covalent assembly to the two stapled superstructures (Figures 3 and S31), suggesting enhanced electronic coupling between PBI chromophores. Our data indicate that the degree of Frenkel exciton and CT mixing within covalently linked superstructures can be modulated *via* choice of an appropriate stapling unit.

Table 1. Excited State Ratio and Lifetimes Obtained from TA

	PBI-Non-Cov	PBI-Stap-13	PBI-Stap-2
^{1}PBI*/PBI$^{\bullet-}$ integrated peak ratio	1.21	1.09	0.79
excited state lifetime (ps)	373 ± 10	406 ± 15	235 ± 10

CONCLUSIONS

We have shown that stapling π-SPs with molecular tethers delivers electronically and structurally well-defined nanoscale objects whose ground- and excited-state electronic properties are governed by the structural characteristic of the tethers. The use of a short, ethylene oxide linker delivers stapled superstructures that feature stable excitonic coupling over a 274-to-368 K temperature range. This result improves upon that previously obtained for superstructures stapled with longer, more flexible polyethylene oxide tethers, which exhibit a decrease in excitonic coupling of more than 18% over an identical temperature range. As excitonic coupling in molecular aggregates is extremely sensitive to conformational changes between electronically coupled units, we posit that the reported tethering strategy is an efficient route to rigidify, post assembly, the redox active cores of π-SPs.

This conclusion is further validated by solution-phase cyclic voltammetry combined with spectroelectrochemistry experiments. Both the non-covalent, control assembly **PBI-Non-Cov** and **PBI-Stap-13** superstructure exhibit irreversible electrochemical signals primarily attributed to (1) structural reorganization upon n-doping and (2) the existence of energetically disparate electronic states originating from structural heterogeneity. In contrast, the reversible redox waves recorded for **PBI-Stap-2** superstructures indicate existence of well-defined electronic states that we attribute to an increase in structural order enforced by **PBI-Stap-2**'s short, rigid tethers. The change in conformational rigidity governed by the molecular tethers is emphasized by examining the excited-state spectroscopic properties and dynamics of PBI superstructures. Notably, the degree of Frenkel exciton and CT contributions to the lowest-energy photoexcited state of each assembly is shown to be intimately related to the conformational freedom of the stapling units, with the highly rigid **PBI-Stap-2** superstructure featuring the highest degree of the CT character.

Taken together, these results underscore that the post-assembly modification of non-covalent assemblies with an adequate stapling unit opens new avenues to (1) deliver

https://doi.org/10.1021/acs.chemmater.2c01353
Chem. Mater. 2022, 34, 6518−6528

covalently bonded superstructures with a tunable degree of conformational rigidity and (2) enforce a high degree of chromophore coupling, at room temperature, without the need of time-consuming and extensive repeating unit syntheses. In addition, the ability to dial-in CT character by design paves the way to engineer redox-active superstructures that readily separate charge upon light absorption, which can enable new materials for solar energy conversion and photocatalysis.

EXPERIMENTAL SECTION

PBI-Stap-2 Superstructures. To a solution of **PBI-C≡CH** (10 mg, 14 μmol) and **PEG$_2$-N$_3$** (16 μmol) in degassed HPLC water (9 mL), a solution of $CuSO_4$ (1.5 mg, 9.3 μmol) and sodium ascorbate (2.4 mg, 12 μmol) in degassed HPLC water (1 mL) was added. The combined solution was stirred at room temperature overnight under Ar. The reaction mixture was then centrifuged in a 10,000 Da MWCO centrifuge filter at 6000 rpm for 10 min repeatedly until the filtrate became colorless. The aqueous solution was subsequently purified on a Sephacryl S200 HR size exclusion column using a buffer solution (50% CH_3CN in H_2O, 0.1 $NaNO_3$). The buffer solution was then desalted using 10,000 Da MWCO centrifuge filter at 6000 rpm for 10 min and pure H_2O. The **PBI-Stap-2** derivative is stable for months, or it can be dried by evaporating the solvent to form a red, glassy film.

Nanoparticle Tracking Analysis. NTA measurements were performed with a LM10 HS (NanoSight, Amesbury, United Kingdom), equipped with a sCMOS camera, sample chamber with a 488 nm blue laser, and Viton fluoroelastomer o-ring. Samples were prepared from concentrated stock solutions of PBI derivatives in buffer solution, diluted to approximately 10 μM using HPLC water and filtered through a 0.45 μm polytetrafluoroethylene syringe filter. Aqueous PBS buffer solution was used as the solvent media to suppress fluorescence coming from residual free PBI units. An initial measurement of buffer solution was collected. No contaminants were detected and, naturally, the total observed number of nanoparticles for the blank solution = 0. The samples were injected into the sample chamber with 1 mL sterile syringes (Restek Corporation, Pennsylvania, USA) until the liquid reached the tip of the nozzle. All measurements were performed at 25 °C using a LM14C temperature controller (NanoSight, Amesbury, United Kingdom). Each sample was measured three times. All measurements shown herein were collected using an instrument-preset 532 nm (green) laser. Measurements obtained using other present wavelengths rendered similar results.

X-ray Photoelectron Spectroscopy. The chemical composition of the stapled superstructure PBI-Stap-2 was interrogated using X-ray photoelectron spectroscopy (XPS) to validate the successful tethering of PBI units with the molecular tether. XPS spectra were recorded for a dried film of PBI-Stap-2 obtained by drop casting an aqueous solution onto an untreated Si/SiO_x substrate followed by drying under ambient conditions and subsequently under high vacuum. XPS data were collected at the Chapel Hill Analytical and Nanofabrication Laboratory (CHANL) at the University of North Carolina, Chapel Hill. The instrumental set up employed a Kratos Axis Ultra DLD system (base pressure = 6×10^{-9} Torr) equipped with a monochromatic Al Kα source. The pass energies for the survey and high-resolution scans were 80 and 20 eV, respectively. Charge compensation was addressed with a charge neutralizer. All spectral data were corrected to the binding energy of the C 1s emission peak at 284.6 eV. Spectral deconvolutions were attained with a Voigt function (30% Lorentzian and 70% Gaussian).

Tapping Mode Atomic Force Microscopy. Tapping mode AFM images were recorded for all functionalized Si surfaces using a Digital Instruments Dimension 3100 microscope (located at the Dr. John T. Macdonald Foundation BioNIUM Institute at the University of Miami). The microscope was operated with a "Nanoscope 6" controller. AFM images were collected in the tapping mode under air at room temperature using silicon tips (n-type, tip radius < 10 nm, f = 43−81 kHz, k = 0.6−3.7 N/m) obtained from AppNano (FORTA-10). The scan rate was typically 0.8 Hz per line. Resultant AFM images were analyzed using Gwyddion software (version 2.51). AFM images were recorded for **PBI-Stap-13** and **PBI-Stap-2** to analyze their solid-state morphologies and gain insights into their thicknesses. Please note the AFM images pertinent to the control **PBI-Non-Cov** assembly were reported previously, but an additional image is shown in Figure S10.[1] The sample in each case was prepared by drop-casting an aqueous solution of the PBI derivative onto a Si surface at room temperature followed by drying under ambient conditions. Shown below are the representative AFM images and pertinent height profile data for **PBI-Stap-13**, **PBI-Stap-2**, and the control non-covalent assemblies **PBI-Non-Cov**.

Electrochemical Measurements. Electrochemical measurements were carried out *via* cyclic voltammetry using a PARSTAT 3000A potentiostat (Ametek Scientific Instruments, USA). For solution-state electrochemical studies, CVs were recorded for aqueous solutions (concentration ∼500 μM) of **PBI-Stap-13**, **PBI-Stap-2**, and the aggregated **PBI-Non-Cov** control using a glassy carbon working electrode (electro-active surface area = 0.071 cm^2), a platinum counter electrode, a Ag/AgCl (3 M NaCl) reference electrode, and sodium chloride (0.025 M) as the supporting electrolyte under an Ar gas atmosphere at room temperature. All potentials are reported against SCE using ferrocenedicarboxylic acid as internal references (Fc/Fc^+ = 0.45 V *vs* SCE).

The CVs in all cases were exploited to determine the cathodic reduction potential of the PBI chromophores in each superstructure. Please note that in each case, the first inflection potential for cathodic reduction was estimated by calculating the first derivative of the current as a function of the applied potential. It should be underscored that to alleviate plausible issues of cross-contamination, unreliable data, and so on, each measurement was reproduced independently (using a new electrochemical setup) *at least* three times.

Spectroelectrochemical Measurements. Spectroelectrochemistry measurements were carried out using a PARSTAT 3000A potentiostat (Ametek Scientific Instruments, USA) and a Cary 5000 UV−vis−NIR spectrophotometer. In a typical experiment, a solution (concentration ∼500 μM, O.D. ∼ 2.5, l = 1.00 mm) of a PBI derivative in D_2O was gently degassed in a 1.00 mm pathlength-modified quartz cell. Subsequently, the cell was equipped with a Au honeycomb electrode that serves both as the working and counter electrodes and a reference electrode (Ag/AgCl, 3 M NaCl). Prior to taking all reported spectra, the potentials were equilibrated for about 10 min or until the applied current plateaued to the smallest possible current (typically $I < -200$ μA). All experiments were conducted under a gentle flow of Ar to prevent oxygen and water contamination. Subsequently, the ground-state electronic absorption spectrum of the PBI solution was recorded followed by a gradual increase in the applied cathodic reduction potential (*i.e.*, more negative) in intervals of 50 mV until achievement of the endpoint of the experiment. It should be noted that by using the ionic nature of the ammonium side chains as part of the PBI derivatives as a leverage, addition of any supporting electrolyte was deemed unnecessary to perform these measurements.

Ultrafast Transient Absorption (TA). TA measurements were performed using the output of a Ti:sapphire regenerative amplifier (3 kHz, ∼90 fs, Coherent Legend Elite Duo) with a center wavelength of 804 nm. Excitation pulses centered at 570 nm were created by sending the 804 nm fundamental output into an optical parametric amplifier (Light Conversion TOPAS-Prime) to produce a pulse centered at 1140 nm that was subsequently passed through a Type-I BBO (Newlight Photonics P/N:BTC10100-SHG800(I)-P) to generate the second harmonic at 570 nm. Spectrally broad probe pulses were produced by focusing a portion of the 804 nm fundamental into a 2 mm thick c-cut sapphire crystal, which yielded a supercontinuum with a spectral bandwidth extending from 440 to 780 nm. Probe light was spectrally dispersed on a 500 mm pathlength Czerny−Turner spectrometer (Acton Instruments SP2500 SpectraPro 2556-i) and collected with a CCD camera (Princeton Instruments PyLoN 100-BR). The relative polarization of the pump and probe were set to the magic angle, 54.7°, to suppress any signal contributions from changes

https://doi.org/10.1021/acs.chemmater.2c01353
Chem. Mater. 2022, 34, 6518−6528

in the orientation of excited species. Solutions of non-covalent and stapled superstructures used for TA were diluted with ultrapure water such that the optical density of the sample was ∼0.1 OD at the excitation wavelength (570 nm) in a 1 mm path length cuvette. Solutions were continuously stirred throughout TA data collection. Measurements were repeated twice using pump pulses with a fluence of ∼100 $\mu J/cm^2$.

■ ASSOCIATED CONTENT

Supporting Information

The Supporting Information is available free of charge at https://pubs.acs.org/doi/10.1021/acs.chemmater.2c01353.

Synthesis and characterization of the **PBI-Stap-2** superstructure precursors, excitonic coupling calculation as a function of temperature for the **PBI-Stap-2** superstructure, AFM and SEM for the **PBI-Stap-2** superstructure, NTA data, NMR and high-resolution MS, XPS, spectroelectrochemistry, electrochemistry, and pump-probe TA spectroscopy (PDF)

■ AUTHOR INFORMATION

Corresponding Authors

Sean T. Roberts − *Department of Chemistry, The University of Texas at Austin, Austin, Texas 78714-1224, United States;* orcid.org/0000-0002-3322-3687; Phone: +1 512-475-9450; Email: roberts@cm.utexas.edu

Jean-Hubert Olivier − *Department of Chemistry, University of Miami, Coral Gables, Florida 33146, United States;* orcid.org/0000-0003-0978-4107; Phone: +1 305-284-3279; Email: jh.olivier@miami.edu

Authors

Victor Paulino − *Department of Chemistry, University of Miami, Coral Gables, Florida 33146, United States;* orcid.org/0000-0001-8916-3604

Danielle M. Cadena − *Department of Chemistry, The University of Texas at Austin, Austin, Texas 78714-1224, United States*

Kaixuan Liu − *Department of Chemistry, University of Miami, Coral Gables, Florida 33146, United States*

Arindam Mukhopadhyay − *Department of Chemistry, University of Miami, Coral Gables, Florida 33146, United States;* orcid.org/0000-0002-0620-4157

Complete contact information is available at: https://pubs.acs.org/10.1021/acs.chemmater.2c01353

Author Contributions

The manuscript was written through contributions of all authors.

Funding

The research conducted at the University of Miami (J.-H.O.) was supported by the National Science Foundation through the CAREER award CHE-1941410. V.P. and J.-H.O. are grateful to the Provost Research Award. S.T.R. and D.M.C. acknowledge support from the Welch Foundation (grant F-1885). S.T.R. additionally acknowledges support from a Sloan Research Fellowship, whereas D.M.C. acknowledges support from a NSF GRFP award (DGE-1610403).

Notes

The authors declare no competing financial interest.

■ ACKNOWLEDGMENTS

We thank Dr. Carrie Donley at the UNC Chapel Hill for performing XPS experiments on the stapled assemblies. The authors are grateful to BioNIUM for providing access to the atomic force microscope and scanning electron microscope. The authors thank Prof. Moon at the Florida International University for his assistance with NTA measurements.

■ REFERENCES

(1) Liu, Z.; Yan, H.; Wang, K.; Kuang, T.; Zhang, J.; Gui, L.; An, X.; Chang, W. Crystal structure of spinach major light-harvesting complex at 2.72 Å resolution. *Nature* **2004**, *428*, 287−292.

(2) Conde, C.; Cáceres, A. Microtubule assembly, organization and dynamics in axons and dendrites. *Nat. Rev. Neurosci.* **2009**, *10*, 319−332.

(3) Bennett, D. I. G.; Amarnath, K.; Fleming, G. R. A Structure-Based Model of Energy Transfer Reveals the Principles of Light Harvesting in Photosystem II Supercomplexes. *J. Am. Chem. Soc.* **2013**, *135*, 9164−9173.

(4) Schlau-Cohen, G. S.; Ishizaki, A.; Calhoun, T. R.; Ginsberg, N. S.; Ballottari, M.; Bassi, R.; Fleming, G. R. Elucidation of the timescales and origins of quantum electronic coherence in LHCII. *Nat. Chem.* **2012**, *4*, 389−395.

(5) Amarnath, K.; Bennett, D. I. G.; Schneider, A. R.; Fleming, G. R. Multiscale model of light harvesting by photosystem II in plants. *Proc. Natl. Acad. Sci. U.S.A.* **2016**, *113*, 1156.

(6) Polizzi, N. F.; Eibling, M. J.; Perez-Aguilar, J. M.; Rawson, J.; Lanci, C. J.; Fry, H. C.; Beratan, D. N.; Saven, J. G.; Therien, M. J. Photoinduced Electron Transfer Elicits a Change in the Static Dielectric Constant of a de Novo Designed Protein. *J. Am. Chem. Soc.* **2016**, *138*, 2130−2133.

(7) Solomon, L. A.; Sykes, M. E.; Wu, Y. A.; Schaller, R. D.; Wiederrecht, G. P.; Fry, H. C. Tailorable Exciton Transport in Doped Peptide-Amphiphile Assemblies. *ACS Nano* **2017**, *11*, 9112−9118.

(8) Anaya-Plaza, E.; Joseph, J.; Bauroth, S.; Wagner, M.; Dolle, C.; Sekita, M.; Gröhn, F.; Spiecker, E.; Clark, T.; de la Escosura, A.; Guldi, D. M.; Torres, T. Synergy of Electrostatic and $\pi-\pi$ Interactions in the Realization of Nanoscale Artificial Photosynthetic Model Systems. *Angew. Chem., Int. Ed.* **2020**, *59*, 18786−18794.

(9) Orłowski, R.; Clark, J. A.; Derr, J. B.; Espinoza, E. M.; Mayther, M. F.; Staszewska-Krajewska, O.; Winkler, J. R.; Jędrzejewska, H.; Szumna, A.; Gray, H. B.; Vullev, V. I.; Gryko, D. T. Role of intramolecular hydrogen bonds in promoting electron flow through amino acid and oligopeptide conjugates. *Proc. Natl. Acad. Sci. U.S.A.* **2021**, *118*, No. e2026462118.

(10) Méndez-Ardoy, A.; Markandeya, N.; Li, X.; Tsai, Y.-T.; Pecastaings, G.; Buffeteau, T.; Maurizot, V.; Muccioli, L.; Castet, F.; Huc, I.; Bassani, D. M. Multi-dimensional charge transport in supramolecular helical foldamer assemblies. *Chem. Sci.* **2017**, *8*, 7251−7257.

(11) Würthner, F.; Saha-Möller, C. R.; Fimmel, B.; Ogi, S.; Leowanawat, P.; Schmidt, D. Perylene Bisimide Dye Assemblies as Archetype Functional Supramolecular Materials. *Chem. Rev.* **2016**, *116*, 962−1052.

(12) Wasielewski, M. R. Self-Assembly Strategies for Integrating Light Harvesting and Charge Separation in Artificial Photosynthetic Systems. *Acc. Chem. Res.* **2009**, *42*, 1910−1921.

(13) Bialas, D.; Kirchner, E.; Röhr, M. I. S.; Würthner, F. Perspectives in Dye Chemistry: A Rational Approach toward Functional Materials by Understanding the Aggregate State. *J. Am. Chem. Soc.* **2021**, *143*, 4500−4518.

(14) Kang, S.; Kim, T.; Hong, Y.; Würthner, F.; Kim, D. Charge-Delocalized State and Coherent Vibrational Dynamics in Rigid PBI H-Aggregates. *J. Am. Chem. Soc.* **2021**, *143*, 9825−9833.

(15) Kaufmann, C.; Bialas, D.; Stolte, M.; Würthner, F. Discrete π-Stacks of Perylene Bisimide Dyes within Folda-Dimers: Insight into Long- and Short-Range Exciton Coupling. *J. Am. Chem. Soc.* **2018**, *140*, 9986−9995.

(16) Hestand, N. J.; Spano, F. C. Molecular Aggregate Photophysics beyond the Kasha Model: Novel Design Principles for Organic Materials. *Acc. Chem. Res.* **2017**, *50*, 341−350.
(17) Hestand, N. J.; Spano, F. C. Expanded Theory of H- and J-Molecular Aggregates: The Effects of Vibronic Coupling and Intermolecular Charge Transfer. *Chem. Rev.* **2018**, *118*, 7069−7163.
(18) Sung, J.; Nowak-Król, A.; Schlosser, F.; Fimmel, B.; Kim, W.; Kim, D.; Würthner, F. Direct Observation of Excimer-Mediated Intramolecular Electron Transfer in a Cofacially-Stacked Perylene Bisimide Pair. *J. Am. Chem. Soc.* **2016**, *138*, 9029−9032.
(19) Kaufmann, C.; Kim, W.; Nowak-Król, A.; Hong, Y.; Kim, D.; Würthner, F. Ultrafast Exciton Delocalization, Localization, and Excimer Formation Dynamics in a Highly Defined Perylene Bisimide Quadruple π-Stack. *J. Am. Chem. Soc.* **2018**, *140*, 4253−4258.
(20) Greyson, E. C.; Vura-Weis, J.; Michl, J.; Ratner, M. A. Maximizing Singlet Fission in Organic Dimers: Theoretical Investigation of Triplet Yield in the Regime of Localized Excitation and Fast Coherent Electron Transfer. *J. Phys. Chem. B* **2010**, *114*, 14168−14177.
(21) Smith, M. B.; Michl, J. Recent Advances in Singlet Fission. *Annu. Rev. Phys. Chem.* **2013**, *64*, 361−386.
(22) Margulies, E. A.; Miller, C. E.; Wu, Y.; Ma, L.; Schatz, G. C.; Young, R. M.; Wasielewski, M. R. Enabling singlet fission by controlling intramolecular charge transfer in π-stacked covalent terrylenediimide dimers. *Nat. Chem.* **2016**, *8*, 1120−1125.
(23) Le, A. K.; Bender, J. A.; Arias, D. H.; Cotton, D. E.; Johnson, J. C.; Roberts, S. T. Singlet Fission Involves an Interplay between Energetic Driving Force and Electronic Coupling in Perylenediimide Films. *J. Am. Chem. Soc.* **2018**, *140*, 814−826.
(24) Young, R. M.; Wasielewski, M. R. Mixed Electronic States in Molecular Dimers: Connecting Singlet Fission, Excimer Formation, and Symmetry-Breaking Charge Transfer. *Acc. Chem. Res.* **2020**, *53*, 1957−1968.
(25) Kellogg, M.; Akil, A.; Muthiah Ravinson, D. S.; Estergreen, L.; Bradforth, S. E.; Thompson, M. E. Symmetry breaking charge transfer as a means to study electron transfer with no driving force. *Faraday Discuss.* **2019**, *216*, 379−394.
(26) Ivanov, A. I.; Dereka, B.; Vauthey, E. A simple model of solvent-induced symmetry-breaking charge transfer in excited quadrupolar molecules. *J. Chem. Phys.* **2017**, *146*, 164306.
(27) Hicks, G. E. J.; Li, S.; Obhi, N. K.; Jarrett-Wilkins, C. N.; Seferos, D. S. Programmable Assembly of π-Conjugated Polymers. *Adv. Mater.* **2021**, *33*, 2006287.
(28) Brunsveld, L.; Folmer, B. J. B.; Meijer, E. W.; Sijbesma, R. P. Supramolecular Polymers. *Chem. Rev.* **2001**, *101*, 4071−4098.
(29) Whitesides, G. M.; Grzybowski, B. Self-Assembly at All Scales. *Science* **2002**, *295*, 2418−2421.
(30) Aida, T.; Meijer, E. W.; Stupp, S. I. Functional Supramolecular Polymers. *Science* **2012**, *335*, 813−817.
(31) Sinha, N. J.; Langenstein, M. G.; Pochan, D. J.; Kloxin, C. J.; Saven, J. G. Peptide Design and Self-assembly into Targeted Nanostructure and Functional Materials. *Chem. Rev.* **2021**, *121*, 13915−13935.
(32) Korevaar, P. A.; Schaefer, C.; de Greef, T. F. A.; Meijer, E. W. Controlling Chemical Self-Assembly by Solvent-Dependent Dynamics. *J. Am. Chem. Soc.* **2012**, *134*, 13482−13491.
(33) Mabesoone, M. F. J.; Markvoort, A. J.; Banno, M.; Yamaguchi, T.; Helmich, F.; Naito, Y.; Yashima, E.; Palmans, A. R. A.; Meijer, E. W. Competing Interactions in Hierarchical Porphyrin Self-Assembly Introduce Robustness in Pathway Complexity. *J. Am. Chem. Soc.* **2018**, *140*, 7810−7819.
(34) Herkert, L.; Droste, J.; Kartha, K. K.; Korevaar, P. A.; de Greef, T. F. A.; Hansen, M. R.; Fernández, G. Pathway Control in Cooperative vs. Anti-Cooperative Supramolecular Polymers. *Angew. Chem., Int. Ed.* **2019**, *58*, 11344−11349.
(35) Smulders, M. M. â. J.; Nieuwenhuizen, M. M. â. L.; deâ€...Greef, T. F. â. A.; vanâ€...derâ€...Schoot, P.; Schenning, A. P. â. H. â. J.; Meijer, E. â. W. How to Distinguish Isodesmic from Cooperative Supramolecular Polymerisation. *Chem.—Eur. J.* **2010**, *16*, 362−367.
(36) Fennel, F.; Wolter, S.; Xie, Z.; Plötz, P.-A.; Kühn, O.; Würthner, F.; Lochbrunner, S. Biphasic Self-Assembly Pathways and Size-Dependent Photophysical Properties of Perylene Bisimide Dye Aggregates. *J. Am. Chem. Soc.* **2013**, *135*, 18722−18725.
(37) De Greef, T. F. A.; Smulders, M. M. J.; Wolffs, M.; Schenning, A. P. H. J.; Sijbesma, R. P.; Meijer, E. W. Supramolecular Polymerization. *Chem. Rev.* **2009**, *109*, 5687−5754.
(38) Lau, Y. H.; de Andrade, P.; Wu, Y.; Spring, D. R. Peptide stapling techniques based on different macrocyclisation chemistries. *Chem. Soc. Rev.* **2015**, *44*, 91−102.
(39) Walensky, L. D.; Bird, G. H. Hydrocarbon-Stapled Peptides: Principles, Practice, and Progress. *J. Med. Chem.* **2014**, *57*, 6275−6288.
(40) Zhang, F.; Sadovski, O.; Xin, S. J.; Woolley, G. A. Stabilization of Folded Peptide and Protein Structures via Distance Matching with a Long, Rigid Cross-Linker. *J. Am. Chem. Soc.* **2007**, *129*, 14154−14155.
(41) Li, X.; Chen, S.; Zhang, W.-D.; Hu, H.-G. Stapled Helical Peptides Bearing Different Anchoring Residues. *Chem. Rev.* **2020**, *120*, 10079−10144.
(42) Blackwell, H. E.; Grubbs, R. H. Highly Efficient Synthesis of Covalently Cross-Linked Peptide Helices by Ring-Closing Metathesis. *Angew. Chem., Int. Ed.* **1998**, *37*, 3281−3284.
(43) Jo, H.; Meinhardt, N.; Wu, Y.; Kulkarni, S.; Hu, X.; Low, K. E.; Davies, P. L.; DeGrado, W. F.; Greenbaum, D. C. Development of α-Helical Calpain Probes by Mimicking a Natural Protein-Protein Interaction. *J. Am. Chem. Soc.* **2012**, *134*, 17704−17713.
(44) Kumita, J. R.; Smart, O. S.; Woolley, G. A. Photo-control of helix content in a short peptide. *Proc. Natl. Acad. Sci. U.S.A.* **2000**, *97*, 3803.
(45) Yamamoto, T.; Fukushima, T.; Yamamoto, Y.; Kosaka, A.; Jin, W.; Ishii, N.; Aida, T. Stabilization of a Kinetically Favored Nanostructure: Surface ROMP of Self-Assembled Conductive Nanocoils from a Norbornene-Appended Hexa-peri-hexabenzocoronene. *J. Am. Chem. Soc.* **2006**, *128*, 14337−14340.
(46) Sato, K.; Ji, W.; Palmer, L. C.; Weber, B.; Barz, M.; Stupp, S. I. Programmable Assembly of Peptide Amphiphile via Noncovalent-to-Covalent Bond Conversion. *J. Am. Chem. Soc.* **2017**, *139*, 8995−9000.
(47) Chin, S. M.; Synatschke, C. V.; Liu, S.; Nap, R. J.; Sather, N. A.; Wang, Q.; Álvarez, Z.; Edelbrock, A. N.; Fyrner, T.; Palmer, L. C.; Szleifer, I.; Olvera de la Cruz, M.; Stupp, S. I. Covalent-supramolecular hybrid polymers as muscle-inspired anisotropic actuators. *Nat. Commun.* **2018**, *9*, 2395.
(48) Rupar, P. A.; Cambridge, G.; Winnik, M. A.; Manners, I. Reversible Cross-Linking of Polyisoprene Coronas in Micelles, Block Comicelles, and Hierarchical Micelle Architectures Using Pt(0)-Olefin Coordination. *J. Am. Chem. Soc.* **2011**, *133*, 16947−16957.
(49) Yamamoto, T.; Fukushima, T.; Kosaka, A.; Jin, W.; Yamamoto, Y.; Ishii, N.; Aida, T. Conductive One-Handed Nanocoils by Coassembly of Hexabenzocoronenes: Control of Morphology and Helical Chirality. *Angew. Chem., Int. Ed.* **2008**, *47*, 1672−1675.
(50) Motoyanagi, J.; Fukushima, T.; Ishii, N.; Aida, T. Photochemical Stitching of a Tubularly Assembled Hexabenzocoronene Amphiphile by Dimerization of Coumarin Pendants. *J. Am. Chem. Soc.* **2006**, *128*, 4220−4221.
(51) Oliver, A. M.; Gwyther, J.; Boott, C. E.; Davis, S.; Pearce, S.; Manners, I. Scalable Fiber-like Micelles and Block Co-micelles by Polymerization-Induced Crystallization-Driven Self-Assembly. *J. Am. Chem. Soc.* **2018**, *140*, 18104−18114.
(52) Zhang, X.; Chen, Z.; Würthner, F. Morphology Control of Fluorescent Nanoaggregates by Co-Self-Assembly of Wedge- and Dumbbell-Shaped Amphiphilic Perylene Bisimides. *J. Am. Chem. Soc.* **2007**, *129*, 4886−4887.
(53) Kim, S. H.; Sun, Y.; Kaplan, J. A.; Grinstaff, M. W.; Parquette, J. R. Photo-crosslinking of a self-assembled coumarin-dipeptide hydrogel. *New J. Chem.* **2015**, *39*, 3225−3228.

https://doi.org/10.1021/acs.chemmater.2c01353
Chem. Mater. 2022, 34, 6518−6528

(54) Ashcraft, A.; Liu, K.; Mukhopadhyay, A.; Paulino, V.; Liu, C.; Bernard, B.; Husainy, D.; Phan, T.; Olivier, J. H. A Molecular Strategy to Lock-in the Conformation of a Perylene Bisimide-Derived Supramolecular Polymer. *Angew. Chem., Int. Ed.* **2020**, *59*, 7487−7493.
(55) Bell, N. C.; Minelli, C.; Tompkins, J.; Stevens, M. M.; Shard, A. G. Emerging Techniques for Submicrometer Particle Sizing Applied to Stöber Silica. *Langmuir* **2012**, *28*, 10860−10872.
(56) Kestens, V.; Bozatzidis, V.; De Temmerman, P.-J.; Ramaye, Y.; Roebben, G. Validation of a particle tracking analysis method for the size determination of nano- and microparticles. *J. Nanoparticle Res.* **2017**, *19*, 271.
(57) Arenas-Guerrero, P.; Delgado, Á. V.; Donovan, K. J.; Scott, K.; Bellini, T.; Mantegazza, F.; Jiménez, M. L. Determination of the size distribution of non-spherical nanoparticles by electric birefringence-based methods. *Sci. Rep.* **2018**, *8*, 9502.
(58) Leira-Iglesias, J.; Sorrenti, A.; Sato, A.; Dunne, P. A.; Hermans, T. M. Supramolecular pathway selection of perylenediimides mediated by chemical fuels. *Chem. Commun.* **2016**, *52*, 9009−9012.
(59) Sorrenti, A.; Leira-Iglesias, J.; Sato, A.; Hermans, T. M. Non-equilibrium steady states in supramolecular polymerization. *Nat. Commun.* **2017**, *8*, 15899.
(60) Walther, A.; Drechsler, M.; Rosenfeldt, S.; Harnau, L.; Ballauff, M.; Abetz, V.; Müller, A. H. E. Self-Assembly of Janus Cylinders into Hierarchical Superstructures. *J. Am. Chem. Soc.* **2009**, *131*, 4720−4728.
(61) Moore, C.; Wing, R.; Pham, T.; Jokerst, J. V. Multispectral Nanoparticle Tracking Analysis for the Real-Time and Label-Free Characterization of Amyloid-β Self-Assembly In Vitro. *Anal. Chem.* **2020**, *92*, 11590−11599.
(62) Zong, S.; Wang, J.; Huang, X.; Wang, T.; Liu, Q.; Tian, B.; Xie, C.; Hao, H. Molecular evolution pathways during nucleation of small organic molecules: solute-rich pre-nucleation species enable control over the nucleation process. *Phys. Chem. Chem. Phys.* **2020**, *22*, 18663−18671.
(63) Brown, K. E.; Salamant, W. A.; Shoer, L. E.; Young, R. M.; Wasielewski, M. R. Direct Observation of Ultrafast Excimer Formation in Covalent Perylenediimide Dimers Using Near-Infrared Transient Absorption Spectroscopy. *J. Phys. Chem. Lett.* **2014**, *5*, 2588−2593.
(64) Chen, Z.; Stepanenko, V.; Dehm, V.; Prins, P.; Siebbeles, L. D. A.; Seibt, J.; Marquetand, P.; Engel, V.; Würthner, F. Photoluminescence and Conductivity of Self-Assembled π-π Stacks of Perylene Bisimide Dyes. *Chem.—Eur. J.* **2007**, *13*, 436−449.
(65) Oleson, A.; Zhu, T.; Dunn, I. S.; Bialas, D.; Bai, Y.; Zhang, W.; Dai, M.; Reichman, D. R.; Tempelaar, R.; Huang, L.; Spano, F. C. Perylene Diimide-Based Hj- and hJ-Aggregates: The Prospect of Exciton Band Shape Engineering in Organic Materials. *J. Phys. Chem. C* **2019**, *123*, 20567−20578.
(66) Kazmaier, P. M.; Hoffmann, R. A Theoretical Study of Crystallochromy. Quantum Interference Effects in the Spectra of Perylene Pigments. *J. Am. Chem. Soc.* **1994**, *116*, 9684−9691.
(67) Vura-Weis, J.; Ratner, M. A.; Wasielewski, M. R. Geometry and Electronic Coupling in Perylenediimide Stacks: Mapping Structure−Charge Transport Relationships. *J. Am. Chem. Soc.* **2010**, *132*, 1738−1739.
(68) Cotton, D. E.; Moon, A. P.; Roberts, S. T. Using Electronic Sum-Frequency Generation to Analyze the Interfacial Structure of Singlet Fission-Capable Perylenediimide Thin Films. *J. Phys. Chem. C* **2020**, *124*, 11401−11413.
(69) Liu, K.; Paulino, V.; Mukhopadhyay, A.; Bernard, B.; Kumbhar, A.; Liu, C.; Olivier, J.-H. How to reprogram the excitonic properties and solid-state morphologies of π-conjugated supramolecular polymers. *Phys. Chem. Chem. Phys.* **2021**, *23*, 2703−2714.
(70) Espinoza, E. M.; Clark, J. A.; Soliman, J.; Derr, J. B.; Morales, M.; Vullev, V. I. Practical aspects of cyclic voltammetry: How to estimate reduction potentials when irreversibility prevails. *J. Electrochem. Soc.* **2019**, *166*, H3175.
(71) Mukhopadhyay, A.; Liu, K.; Paulino, V.; Donley, C. L.; Olivier, J.-H. Silicon Electrodes Functionalized with Perylene Bisimide π-Aggregates for Redox-Controlled Stabilization of Semiconducting Nanointerfaces. *ACS Appl. Nano Mater.* **2021**, *4*, 8813−8822.
(72) Liu, K.; Levy, A.; Liu, C.; Olivier, J.-H. Tuning Structure-Function Properties of π-Conjugated Superstructures by Redox-Assisted Self-Assembly. *Chem. Mater.* **2018**, *30*, 2143−2150.
(73) Liu, K.; Mukhopadhyay, A.; Ashcraft, A.; Liu, C.; Levy, A.; Blackwelder, P.; Olivier, J.-H. Reconfiguration of π-conjugated superstructures enabled by redox-assisted assembly. *Chem. Commun.* **2019**, *55*, 5603−5606.
(74) Wu, Y.; Frasconi, M.; Gardner, D. M.; McGonigal, P. R.; Schneebeli, S. T.; Wasielewski, M. R.; Stoddart, J. F. Electron Delocalization in a Rigid Cofacial Naphthalene-1,8:4,5-bis-(dicarboximide) Dimer. *Angew. Chem., Int. Ed.* **2014**, *53*, 9476−9481.
(75) Takai, A.; Yasuda, T.; Ishizuka, T.; Kojima, T.; Takeuchi, M. A Directly Linked Ferrocene-Naphthalenediimide Conjugate: Precise Control of Stacking Structures of π-Systems by Redox Stimuli. *Angew. Chem., Int. Ed.* **2013**, *52*, 9167−9171.
(76) Penneau, J. F.; Stallman, B. J.; Kasai, P. H.; Miller, L. L. An imide anion radical that dimerizes and assembles into .pi.-stacks in solution. *Chem. Mater.* **1991**, *3*, 791−796.
(77) Paulino, V.; Mukhopadhyay, A.; Tsironi, I.; Liu, K.; Husainy, D.; Liu, C.; Meier, K.; Olivier, J.-H. Molecular Engineering of Water-Soluble Oligomers to Elucidate Radical π-Anion Interactions in n-Doped Nanoscale Objects. *J. Phys. Chem. C* **2021**, *125*, 10526−10538.
(78) Shirman, E.; Ustinov, A.; Ben-Shitrit, N.; Weissman, H.; Iron, M. A.; Cohen, R.; Rybtchinski, B. Stable Aromatic Dianion in Water. *J. Phys. Chem. B* **2008**, *112*, 8855−8858.
(79) Zeman, C. J.; Kim, S.; Zhang, F.; Schanze, K. S. Direct Observation of the Reduction of Aryl Halides by a Photoexcited Perylene Diimide Radical Anion. *J. Am. Chem. Soc.* **2020**, *142*, 2204−2207.
(80) Ahrens, M. J.; Kelley, R. F.; Dance, Z. E. X.; Wasielewski, M. R. Photoinduced charge separation in self-assembled cofacial pentamers of zinc-5,10,15,20-tetrakis(perylenediimide)porphyrin. *Phys. Chem. Chem. Phys.* **2007**, *9*, 1469−1478.
(81) Supur, M.; Fukuzumi, S. Photodriven Electron Transport within the Columnar Perylenediimide Nanostructures Self-Assembled with Sulfonated Porphyrins in Water. *J. Phys. Chem. C* **2012**, *116*, 23274−23282.
(82) Nagarajan, K.; Mallia, A. R.; Reddy, V. S.; Hariharan, M. Access to Triplet Excited State in Core-Twisted Perylenediimide. *J. Phys. Chem. C* **2016**, *120*, 8443−8450.

https://doi.org/10.1021/acs.chemmater.2c01353
Chem. Mater. 2022, 34, 6518−6528